Molecular dynamics simulations with machine learning potential for Nb-doped lithium garnet-type oxide $Li_{7-x}La_3(Zr_{2-x}Nb_x)O_{12}$

Kazutoshi Miwa* and Ryoji Asahi
Toyota Central Research & Development Laboratories, Inc., Nagakute 480-1192, Japan

(Received 19 July 2018; published 24 October 2018)

Lithium garnet-type oxide $Li_7La_3Zr_2O_{12}$ (LLZO) is one of the most promising solid electrolyte materials. In this study, the Li conduction properties of Nb-doped LLZO, $Li_{6.75}La_3(Zr_{1.75}Nb_{0.25})O_{12}$, have been investigated by molecular dynamics simulations with the machine learning potential. It is shown that Nb-doped LLZO holds a high-conductivity cubic structure at low temperatures. Two kinds of Li occupation sites, 24*d* and 96*h*, are correctly predicted, which form the three-dimensional network of the Li migration pathway. The Li conductivity at 298 K and the activation energy are obtained as $\sigma_{Li} = 5.0 \times 10^{-3}$ S/cm and $E_a = 223$ meV, respectively, which are in reasonably good agreement with the experimental data. The free energy difference between the 24*d* and 96*h* sites is expected to be negligibly small. This most likely contributes a high Li conductivity in the Nb-doped LLZO. The Nb substitution for Zr is accompanied with the Li vacancy formation due to the charge neutrality condition, which stabilizes the cubic phase and enhance the Li conduction. The Nb substitution, however, also has a negative effect. The supervalency of the Nb^{5+} ion destabilizes the Li atoms at the surrounding 96*h* sites. The Li conductivity in Nb-doped LLZO is determined by trading off between these effects.

DOI: 10.1103/PhysRevMaterials.2.105404

I. INTRODUCTION

Lithium-ion conductors have attracted great attention because of their potential application for solid electrolytes in all-solid-state batteries. The garnet-type oxide $Li_7La_3Zr_2O_{12}$ (LLZO) is one of the most promising materials [1], which possesses desired features, relatively high ion conductivity, negligible electronic transport, high chemical stability, and a wide energy potential window. For LLZO, many experimental efforts have been made to identify Li conduction properties and improve them [2–7].

It has been known that two polymorphs exist for LLZO, tetragonal and cubic phases [2,3]. The Li conductivity of the tetragonal phase is rather poor ($\sim 10^{-6}$ S/cm at room temperature), while the cubic phase shows a good conductivity, typically 2 orders of magnitude higher than the tetragonal phase. Figure 1(a) indicates the crystal structure of cubic LLZO. This phase has a body-centered cubic (bcc) primitive cell with the symmetry of space group $Ia\bar{3}d$ (No. 230). The La and Zr atoms are located at the 16*a* and 24*c* sites and form LaO_8 dodecahedra and ZrO_6 octahedra, respectively. The Li atoms occupy the tetrahedral 24*d* and octahedral 48*g* sites, where the latter is actually split into two 96*h* sites [3]. These Li sites are partially occupied and form the three-dimensional network as shown in Fig. 1(b), which is thought to be the main feature responsible for the high Li-ion conductivity in the cubic phase. In contrast, the tetragonal phase shows the complete ordering of Li atoms, where the symmetry is reduced to $I4_1/acd$ (No. 142). This reduction transforms the cubic 24*d* sites into the 8*a* and 16*e* sites, and the cubic 48*g*/96*h* sites into the 16*f* and 32*g* sites. The 16*e* site in the tetragonal phase becomes completely vacant, and other 8*a*, 16*f*, and 32*g* sites are fully occupied, forming the ordered arrangement shown in Fig. 1(c).

The stoichiometric LLZO has the tetragonal structure at room temperature and the cubic modification only occurs at elevated temperatures. The phase-transition temperature of contamination-free LLZO has been reported to be around 650 K [7]. Thus, in practical applications, the cubic phase is stabilized by aliovalent substitution. Ohta *et al.* [4] have shown that Nb substitution for Zr considerably improves the Li-ion conductivity. The Nb substitution is accompanied with Li vacancy formation owing to the charge neutrality condition, which disturbs the Li ordering in the tetragonal structure and stabilizes the cubic phase. In addition, an increase in the Li vacant sites is expected to enhance the Li conduction. The Nb-doped compound $Li_{7-x}La_3(Zr_{2-x}Nb_x)O_{12}$, however, exhibits the maximum conductivity at $x = 0.25$ and further doping causes rather deterioration of the conductivity. A similar trend has been found for Ta-doped LLZO [5]. The effects of the supervalent substitution for the Li-ion conduction are still not fully understood.

First-principles calculations based on density functional theory (DFT) [8,9] have been also applied for LLZO. Because of the Li disordering in cubic LLZO, the dynamical correlation most likely plays an important role. In order to take this effect into account, *ab initio* molecular dynamics (MD) simulations have been carried out to investigate the Li conduction properties [10–12]. However, the statistics were taken under limited conditions, high temperatures with relatively small computational cells, due to the high computational demands of DFT.

In this study, we perform the MD simulations with the machine learning potential (MLP) for Nb-doped LLZO. Our recent studies [13,14] have indicated that the MLP approach

*miwa@cmp.tytlabs.co.jp

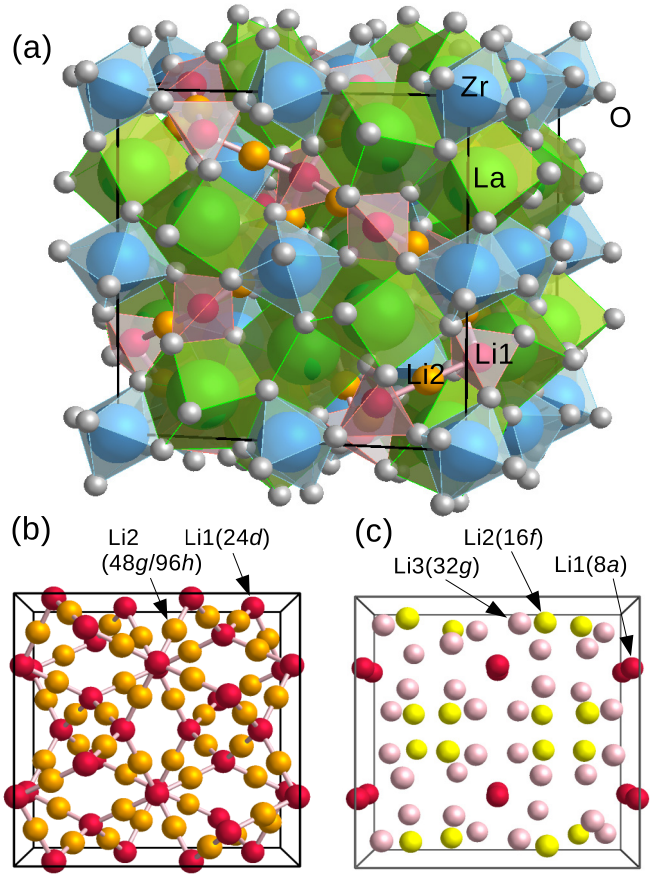

FIG. 1. (a) Crystal structure of cubic LLZO. Green, blue, and gray spheres represent La, Zr, and O atoms, and red and orange spheres indicate Li atoms located at the 24*d* and 48*g*/96*h* sites, respectively. (b) Three-dimensional network formed by Li occupation sites in cubic LLZO. (c) Ordered Li atomic arrangement in the low-temperature tetragonal phase.

allows the large-scale simulations with accuracy comparable to DFT. One of our purposes is to demonstrate the utility of our MLP for Li oxide conductors. The other is to investigate the Li conduction properties, in particular, the effect of the Nb substitution for Zr in LLZO.

II. METHODOLOGY

The machine learning potential for $Li_{6.75}La_3(Zr_{1.75}Nb_{0.25})O_{12}$ (Nb-doped LLZO with $x = 0.25$) has been constructed by the Self-Learning and Adaptive Database (SLAD) approach given in Ref. [14]. In the SLAD, the sample structures for training are collected by the MD simulations using the MLP itself with the aid of the spilling factor for simultaneous error estimation [13].

Here, we briefly summarize the formulation of our MLP. The details can be found in Refs. [13,14]. The geometry around the Ith atom located at $\boldsymbol{R}_I$ is represented by the following descriptor:

$$\boldsymbol{g}^I = g^I_{tt'nl} = \sum_{m=-l}^{l} f^I_{tnlm} f^I_{t'nlm}, \tag{1}$$

TABLE I. Parameters for MLP construction and results of cross validation (CV): the scale parameter θ, regularization parameter λ, fractional ionicity f_z, maximum absolute errors MAE, descriptor expansion parameters, $n_{\max}$ and $l_{\max}$, cutoff radius $R_{\rm cut}$, normalization parameters $\mathcal{D}^{-1}$, spilling factor criteria $s_{\rm large}$ and $s_{\rm huge}$, and recursive bisection criterion δr^2.

	SLAD	Fivefold CV
θ	0.5	0.968
λ	1×10^{-3}	5.5×10^{-4}
f_z	1	0.692
$\mathrm{MAE}_{\rm energy}$ (hartree/atom)	4.3×10^{-4}	4.0×10^{-4}
$\mathrm{MAE}_{\rm force}$ (hartree/bohr)	5.1×10^{-3}	4.5×10^{-3}
$\mathrm{MAE}_{\rm stress}$ (GPa)	0.15	0.10
$n_{\max}$	12	
$l_{\max}$	6	
$R_{\rm cut}$ (bohr)	10	
$\mathcal{D}^{-1}_{\rm energy}$ (hartree/atom)	1×10^{-4}	
$\mathcal{D}^{-1}_{\rm force}$ (hartree/bohr)	1×10^{-3}	
$\mathcal{D}^{-1}_{\rm stress}$ (GPa)	0.1	
$s_{\rm large}$	0.02	
$s_{\rm huge}$	0.04	
δr^2	0.05	

with

$$f^I_{tnlm} = {\sum_{i\in t}}' f_{\rm cut}\left(R^I_i\right) j_l\left(q_n R^I_i\right) Y_{lm}\left(\hat{\boldsymbol{R}}^I_i\right), \tag{2}$$

where $\boldsymbol{R}^I_i = \boldsymbol{R}_i - \boldsymbol{R}_I$, $R^I_i = |\boldsymbol{R}^I_i|$, j_l are the spherical Bessel functions, Y_{lm} are the real spherical harmonics, t are indices for atom types, and $f_{\rm cut}$ is a smooth radial cutoff function with compact support. The prime in the summation of Eq. (2) excludes the $i = I$ term. The sampling wave-vector lengths are set to be $q_n = 2\pi n/R_{\rm cut}$, where $R_{\rm cut}$ is a cutoff radius of $f_{\rm cut}$. The similarity measure between two local geometries is given by

$$d^2(I,J) = \sum_n \sum_l \sum_t \sum_{t'\leqslant t} \left| g^I_{tt'nl} - g^J_{tt'nl} \right|^2, \tag{3}$$

when the Ith and Jth atoms belong to the same atom type; otherwise, $d^2(I,J) = \infty$. Using the similarity measures, the energy is written as a sum of weighted Gaussians:

$$E_{\rm MLP} = \sum_{J\in{\rm ref}} \alpha_J \sum_I \mathcal{Q}(\boldsymbol{g}^I, \boldsymbol{g}^J), \tag{4}$$

where $\mathcal{Q}(\boldsymbol{g}^I, \boldsymbol{g}^J) = \exp[-d^2(I,J)/(2\theta^2)]$, α are the regression coefficients, θ are the scale parameters, and J runs over the reference descriptors. The reference descriptors are constructed from a DFT sample data set using the recursive bisection method. The spilling factor for the error estimation is defined as

$$s(\boldsymbol{g}) = 1 - \sum_{I\in{\rm ref}} \sum_{J\in{\rm ref}} \mathcal{Q}(\boldsymbol{g}, \boldsymbol{g}^I) \mathcal{Q}^{-1}(\boldsymbol{g}^I, \boldsymbol{g}^J) \mathcal{Q}(\boldsymbol{g}^J, \boldsymbol{g}), \tag{5}$$

which is zero when the geometry $\boldsymbol{g}$ is fully projected by the reference descriptors, whereas $s = 1$ when $\boldsymbol{g}$ has no overlaps between them.

Because of an ionic character of the compound, the total energy is divided into the long-range Coulomb

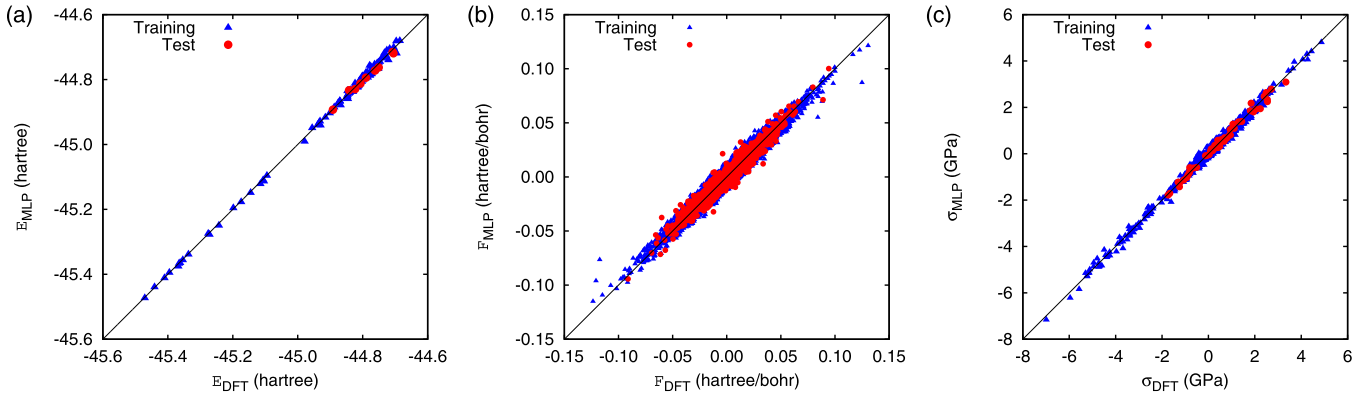

FIG. 2. Comparison between MLP and DFT results: (a) total energy, (b) force, and (c) macroscopic stress.

interaction part and the remaining short-range one. The former is calculated by the Ewald summation with the effective charges $Z_{\rm eff} = f_z Z$, where Z is a nominal valency of each atom (+1, +3, +4, +5, and −2 for Li, La, Zr, Nb, and O) and f_z is the fractional ionicity parameter [15]. During the SLAD iteration, we assume that f_z is unity. The short-range part is represented by $E_{\rm MLP}$ of Eq. (4). The parameters for the MLP construction are summarized in Table I.

The MD structure sampling with the MLP is carried out for the conventional unit cell composed of eight formula units (190 atoms) using the isotherm-isobaric ensemble [16–18]. Temperature and pressure are controlled to be $T =$ 800 K and $P = 0$ GPa, respectively. The tetragonal LLZO structure is chosen as the initial configuration, in which two of 16 Zr atoms located at (0, 0, 0) and (1/2, 1/2, 1/2) are replaced by Nb atoms. Two Li atoms to be removed are randomly selected at the beginning of each MD run. The time step is 0.97 fs and the target MD period is set to 10 000 steps. To prevent large thermal fluctuation, the velocity scaling method is applied for 500 MD steps before starting the isothermal-isobaric MD calculation. DFT calculations for collected sample structures are performed with the ultrasoft pseudopotential method [19,20]. The Brillouin zone integration is performed with single Γ-point sampling, and the cutoff energies are set to be 15 and 120 hartrees for the wave function and charge density, respectively. The generalized gradient approximation proposed by Wu and Cohen [21] is adopted for the exchange-correlation energy.

The SLAD process is completed with 36 iterations. Using the collected DFT sample data set, the scale and regularization parameters as well as the fractional ionicity f_z are refined by the fivefold cross validation. This refinement reduces the maximum absolute errors of the MLP modestly as given in Table I. Figure 2 shows the comparison between the DFT and MLP results. The agreement between them is fairly good [22]. The sample data set consists of 105 structures which contain 19 950 local atomic geometries. From them, 9002 reference descriptors are generated by the recursive bisection method [13].

It is found that the obtained MLP is useful for stoichiometric LLZO, too. Table II shows the crystallographic parameters of tetragonal LLZO optimized by the MLP, which are in good agreement with those by DFT. Both the theoretical results agree well with the experimental data [6]. We also have performed the additional validation [22], which indicates that the present MLP is transferable for stoichiometric LLZO. It is most likely because the DFT sample data set includes adequate local atomic geometries which do not contain Nb atoms (about 45% atoms are outside the Nb cutoff sphere). The present MLP is also applied for undoped LLZO systems in Sec. III for comparison purposes.

III. RESULTS AND DISCUSSION

A. Li conduction in Nb-doped LLZO

Using the constructed MLP, the isothermal-isobaric MD simulations are carried out for Nb-doped LLZO with $x =$ 0.25 to investigate the Li diffusion properties. The $2 \times 2 \times 2$ supercell containing 64 formula units (1520 atoms) is used, where the ordered body-centered sublattice is assumed for the Nb arrangement as done in the MLP construction. The temperature range is set to $T = 400 \sim 800$ K with an interval of 100 K and the target pressure is fixed at $P = 0$ GPa. The MD period is taken to be 50 000 steps for $T \geqslant 600$ K and 90 000 steps for $T \leqslant 500$ K. At each temperature, the first 10 000 MD steps are for equilibration and the remaining steps are used to collect the statistics. For the temperature range considered here, the time-averaged structures of Nb-doped

TABLE II. Crystallographic parameters of tetragonal LLZO. Space group: $I4_1/acd$ (No. 142). The lattice constants obtained by MLP are $a = 13.027$ Å and $c = 12.514$ Å, and those by DFT are $a = 13.010$ Å and $c = 12.535$ Å.

	Wyckoff	MLP			DFT		
Atom	position	x	y	z	x	y	z
Li1	8*a*	0	1/4	3/8	0	1/4	3/8
Li2	16*f*	0.1808	0.4308	1/8	0.1805	0.4305	1/8
Li3	32*g*	0.0805	0.0876	0.8052	0.0793	0.0880	0.8091
La1	8*b*	0	1/4	1/8	0	1/4	1/8
La2	16*e*	0.1274	0	1/4	0.1276	0	1/4
Zr	16*c*	0	0	0	0	0	0
O1	32*g*	0.9652	0.0557	0.1537	0.9657	0.0555	0.1535
O2	32*g*	0.0552	0.8522	0.5346	0.0552	0.8523	0.5350
O3	32*g*	0.1506	0.0277	0.4463	0.1507	0.0280	0.4464

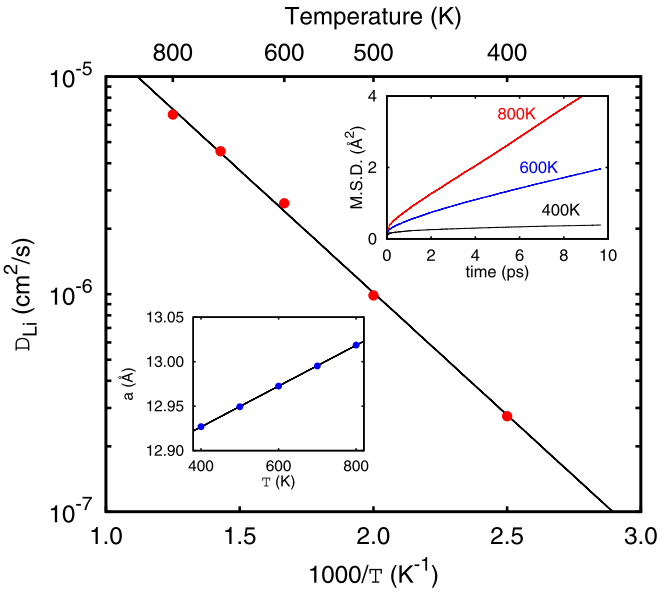

FIG. 3. Arrhenius plot of calculated Li diffusion coefficients D_{Li} for Nb-doped LLZO. The upper inset shows the mean-squared displacement of Li, which is obtained by the overlapped data collection with time interval of 9.7 ps. The lower inset indicates the time-averaged lattice constant as a function of temperature.

LLZO are predicted to be cubic: The deviations of three axial lengths from the geometric mean are less than 0.5%.

Figure 3 depicts the Arrhenius plot of the Li diffusion coefficients D_{Li} calculated from the mean-squared displacement. The predicted D_{Li} are represented well by the Arrhenius equation $D_{\mathrm{Li}} = D^0_{\mathrm{Li}} \exp[-E_a/k_BT]$ with the prefactor $D^0_{\mathrm{Li}} = 1.8 \times 10^{-4}$ cm^2/s and the activation energy $E_a = 223$ meV. The extrapolation according to this relations yields $D_{\mathrm{Li}} = 3.2 \times 10^{-8}$ cm^2/s at 298 K [23]. The lattice constant a as a function of temperature is also shown in Fig. 3, which obeys a linear relationship. The lattice constant at 298 K is extrapolated to $a = 12.90$ Å, which agrees well with the experimental value of 12.95 Å [4]. Using the Nernst-Einstein relation with these extrapolated data, the Li ion conductivity at 298 K is obtained to be $\sigma_{\mathrm{Li}} = 5.0 \times 10^{-3}$ S/cm. The experimental values of the conductivity and the activation energy are $\sigma_{\mathrm{Li}} = 0.8 \times 10^{-3}$ S/cm and $E_a = 310$ meV, respectively [4]. Considering the inevitable contribution from grain boundaries in the experimental measurement [24], the agreement between the prediction and the experiment is thought to be reasonably good. Assuming $\ell = 2$ Å for the average Li hopping distance (approximately a half of the distance between the neighboring 24d sites), the Li hopping frequency is estimated as $\nu = 6D^0_{\mathrm{Li}}/\ell^2 = 2.7$ ps^{-1}.

From the atom trajectories, we calculate the atom density function for Li. All Li trajectories are folded into the bcc primitive cell and the atom positions are mapped onto 100^3 uniform grid points. The cumulative values on the grid points are suitably normalized. The atom density function ρ_{Li} at 600 K is depicted in Fig. 4(a). The three-dimensional network shown in Fig. 1(b) is clearly visible. For comparison, we carry out the MD simulation for the stoichiometric compound $Li_7La_3Zr_2O_{12}$ at 600 K. The structure is predicted to be

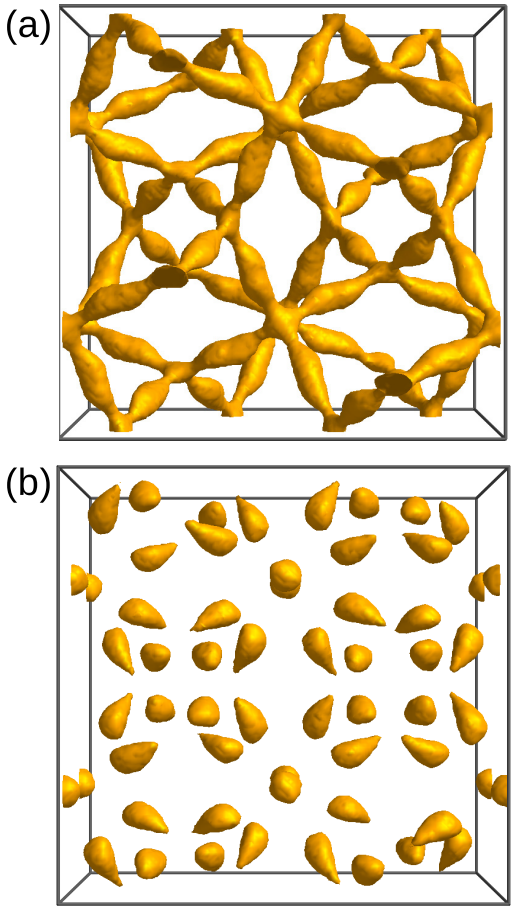

FIG. 4. Isosurface plots of the Li atom density function for (a) Nb-doped LLZO and (b) stoichiometric LLZO at $T = 600$ K. The isovalue is taken to be 0.02 bohr^{-3}.

tetragonal with the lattice parameters $a = 13.13$ Å and $c/a = 0.968$. The obtained ρ_{Li} is plotted in Fig. 4(b), from which the ordered arrangement given in Fig. 1(c) can be confirmed. For this tetragonal phase, any Li migration channels are not connected and the calculated conductivity is negligibly low ($D_{\mathrm{Li}} = 1 \times 10^{-9}$ cm^2/s).

The atom density function can be converted to the free energy difference [25],

$$\Delta F = -k_BT \log\left[\frac{\rho_{\mathrm{Li}}}{\rho^0_{\mathrm{Li}}}\right], \tag{6}$$

where ρ^0_{Li} indicates the density at the reference point. Here, we choose the tetrahedral 24d site as the reference and the density is symmetrized with the $Ia\bar{3}d$ symmetry operations to remedy statistical errors. In this analysis, therefore, the effect of the Nb substitution for Zr is taken into consideration in an average manner. The potential energy surface is analyzed to determine the minimum energy path for Li migration between the neighboring 24d sites in the cubic phase. The results at 600 K are given in Fig. 5. Around the 48g site at the middle of the pathway, the 96h site pair is correctly reproduced. The pair is separated by a tiny energy barrier of 17 meV at the 48g site. The predicted position of the 96h site is (0.097, 0.688, 0.576) which agrees well with the experimental one for Ta-doped

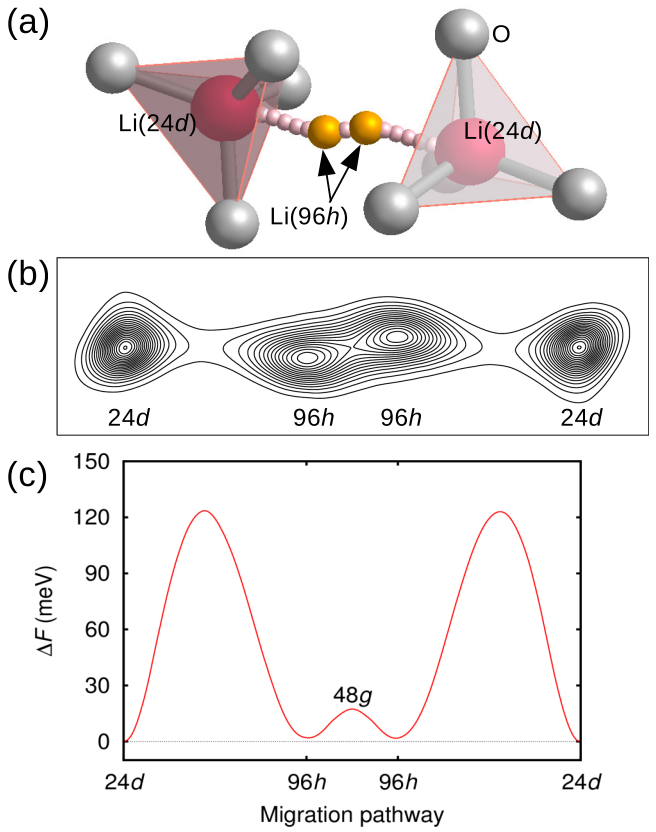

FIG. 5. Minimum energy path for Li migration between the neighboring 24*d* sites. (a) Three-dimensional view. (b) Contour plot of the Li atom density function. The contour spacing is 0.03 bohr^{-3}. (c) Free energy profile along the migration pathway.

LLZO, (0.099, 0.686, 0.580) [6]. The major energy barrier is found between the 24*d* and adjacent 96*h* sites with the height of 124 meV. The free energy difference between the 24*d* and 96*h* sites is predicted to be nearly zero.

The temperature dependence of the free energy profile along the Li migration pathway is marginal. The free energy differences at the saddle point, 48*g*, and 96*h* sites as a function of temperature are plotted in Fig. 6. The energy at the 96*h* site is essentially unchanged and kept to be nearly zero. The Li occupancies of the 24*d* and 96*h* sites are, therefore, expected to be almost equal, whose value will be $n_{\rm occ} \simeq 0.45$ ($= 54/120$). The energy barrier at the saddle point decreases slightly with decreasing temperature, whereas the energy at the 48*g* site shows a small increase.

The saddle-point barrier height calculated from the atom density function is about 120 meV, which is lower than $E_a = 223$ meV obtained from the Arrhenius plot. The former approach is based on the mean-field approximation, which reduces the effect of the correlation between Li atoms to the effective one-body potential and becomes correct in a Li dilute limit. In the latter, the correlation is taken into account more exactly in a statistical way. The difference between two approaches suggests that the Li-Li correlation plays an important role for the Li conduction in LLZO.

Figure 7 depicts the pair radial distribution functions (RDFs) at 600 K. In the Li-Li RDF plot, there are no

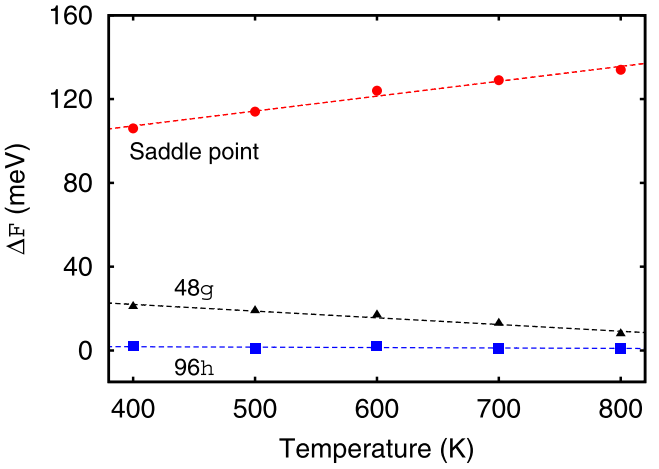

FIG. 6. Free energy differences at the saddle point, 48*g*, and 96*h* sites as a function of temperature. The dotted lines are added as eye-guides.

peaks at the radial distance $r < 2$ Å. This indicates that it is forbidden to simultaneously occupy the 24*d* and adjacent 96*h* sites whose interatomic distance is $d = 1.7$ Å, probably because of the cationic repulsion. The first-peak position ($r = 2.5$ Å) approximately coincides with the distance between the second-nearest neighboring 24*d*-96*h* sites ($d = 2.3$ Å). For the Zr-O and Nb-O pairs, the Nb-O bond length is shorter than the Zr-O one, reflecting the difference of the ionic radii of cations, Zr^{4+} (0.79 Å) and Nb^{5+} (0.69 Å). The first peak of the Zr-Li PDF is located at 3.0 Å, which corresponds to the Zr-Li(96*h*) pair ($d = 2.9, 3.1$ Å). The Nb-Li PDF shows a

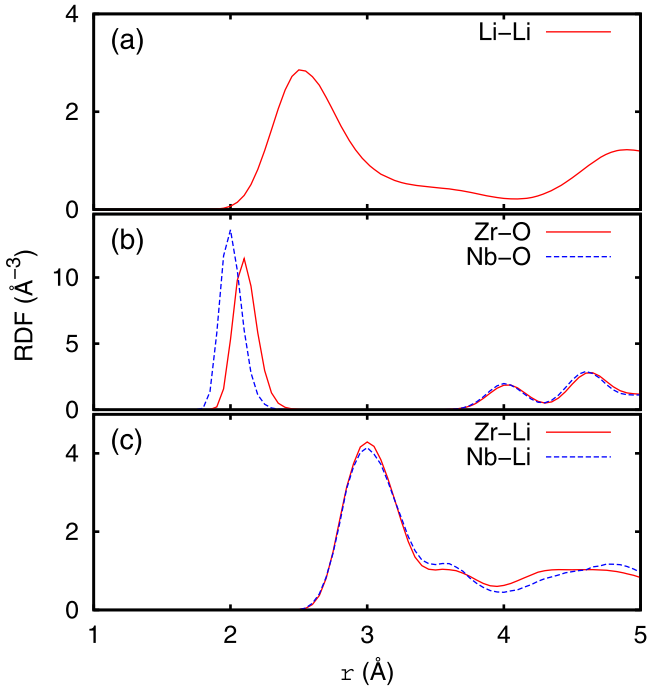

FIG. 7. Pair radial distribution functions for (a) Li-Li, (b) Zr(Nb)-O, and (c) Zr(Nb)-Li in Nb-doped LLZO at 600 K.

similar distribution, but the height of its first peak is slightly lower than that of the Zr-Li PDF.

B. Effects of Nb substitution

As mentioned in Sec. I, the Li vacancy formation is expected to be the major effect of the Nb substitution for Zr, which stabilizes the cubic phase and enhances the Li conduction. Our results given in Figs. 4(a) and 4(b) support this consideration. However, the enhancement effect saturates with a relatively small amount of the substitution, $x = 0.25$ [4]. This implies that the Nb substitution also has a negative effect for the Li conduction, and the conductivity is determined by trading off between both effects. The Zr(Nb)-Li RDF given in Fig. 7(c) suggests that the Nb atom destabilizes the Li atoms at the surrounding 96*h* sites.

In order to separate the enhancement effect caused by Li vacancies from the Nb-substitution contribution, we consider the hypothetical compound, undoped LLZO, with the Li vacancy concentration $x = 0.25$, $Li_{6.75}La_3Zr_2O_{12}$. The MD simulation is performed for this model compound at 600 K, where the excess negative charges are compensated by the uniform background charge density. The structure is obtained to be cubic. The Li diffusion coefficient is predicted as $D_{Li} = 2.9 \times 10^{-6}$ cm^2/s, which is 12% higher than the value of Nb-doped LLZO, 2.6×10^{-6} cm^2/s. This provides clear evidence for the negative effect of the Nb substitution.

In Ref. [10], *ab initio* MD simulations have been performed for model LLZO. Though the Li conductivities are not reported, it is indicated that the phase-transition temperature monotonically decreases with increasing the Li vacancy concentration up to $x = 0.5$ and shows no saturation. This also supports the negative effect for the aliovalent substitution.

A smaller ionic radius of Nb^{5+} might be the source of this effect. However, the time-averaged lattice constants of Nb-doped and model LLZO are 12.972 and 12.976 Å, respectively, which are quite close to each other. We also investigate the Li migration pathway from a geometrical viewpoint. Throughout the pathway, the narrowest part of the void channel is expected to be the triangle surfaces forming Li(24*d*)-O_4 tetrahedra [see Fig. 5(a)]. The radii of inscribed circles for these triangles are evaluated from the MD profiles. They are represented well by the normal distribution. The mean in radii (the standard deviation) for Nb-doped and model LLZO are obtained to be 0.898 and 0.897 Å (0.028 and 0.028 Å), respectively, indicating that the Li migration channel is geometrically unaffected by the Nb atoms. Thus, it is expected that the negative effect for the Li conduction mainly originates from the supervalency of the Nb^{5+} ion, which destabilizes the Li atoms at the surrounding 96*h* sites due to the electrostatic repulsive interaction.

IV. SUMMARY

The Li conduction properties of Nb-doped garnet-type oxide $Li_{6.75}La_3(Zr_{1.75}Nb_{0.25})O_{12}$ are investigated by the molecular dynamics simulations with the machine learning potential. The Li conductivity at 298 K and the activation energy are predicted as $\sigma_{Li} = 5.0 \times 10^{-3}$ S/cm and $E_a = 223$ meV, respectively, which are in reasonably good agreement with the experimental data. The MD simulations correctly predict two kinds of Li occupation sites, 24*d* and 96*h*, which form the three-dimensional network of the Li migration pathway. Our MLP approach successfully reproduces the Li conduction properties of the LLZO observed experimentally. The free energy difference between the 24*d* and 96*h* sites is expected to be negligibly small. This most likely contributes a high Li conductivity in the Nb-doped LLZO.

Unlike stoichiometric LLZO, Nb-doped LLZO holds a cubic structure at low temperatures. The Nb substitution for Zr stabilizes the cubic phase due to the accompanied Li vacancies which disturb the ordered Li arrangement in the tetragonal phase and enhance the Li conduction. Our analysis, however, reveals that the Nb substitution also has a negative effect. The supervalency of the Nb^{5+} ion destabilizes the Li atoms at the surrounding 96*h* sites. The Li conductivity in Nb-doped LLZO is determined by trading off between both effects.

ACKNOWLEDGMENTS

We are grateful to S. Ohta for informing us about the experimental details. We also thank J. Lee and K. Sato for valuable discussions.

[1] R. Murugan, V. Thangadurai, and W. Weppner, Angew. Chem., Int. Ed. **46**, 7778 (2007).
[2] J. Awaka, N. Kijima, H. Hayakawa, and J. Akimoto, J. Solid State Chem. **182**, 2046 (2009).
[3] J. Awaka, K. Kataoka, N. Kijima, Y. Idemoto, and J. Akimoto, Chem. Lett. **40**, 60 (2011).
[4] S. Ohta, T. Kobayashi, and T. Asaoka, J. Power Sources **196**, 3342 (2011).
[5] H. Buschmann, S. Berendts, B. Mogwitz, and J. Janek, J. Power Sources **206**, 236 (2012).
[6] A. Logéat, T. Köhler, U. Eisele, B. Stiaszny, A. Harzer, M. Tovar, A. Senyshyn, H. Ehrenberg, and B. Kozinsky, Solid State Ionics **206**, 33 (2012).
[7] M. Matsui, K. Sakamoto, A. Hirano, Y. Takeda, O. Yamamoto, and N. Imanishi, Dalton Trans. **43**, 1019 (2014).
[8] P. Hohenberg and W. Kohn, Phys. Rev. **136**, B864 (1964).
[9] W. Kohn and L. J. Sham, Phys. Rev. **140**, A1133 (1965).
[10] N. Bernstein, M. D. Johannes, and K. Hoang, Phys. Rev. Lett. **109**, 205702 (2012).
[11] R. Jalem, Y. Yamamoto, H. Shiba, M. Nakayama, H. Munakata, T. Kasuga, and K. Kanamura, Chem. Mater. **25**, 425 (2013).
[12] L. J. Miara, S. P. Ong, Y. Mo, W. D. Richards, Y. Park, J.-M. Lee, H. S. Lee, and G. Ceder, Chem. Mater. **25**, 3048 (2013).
[13] K. Miwa and H. Ohno, Phys. Rev. B **94**, 184109 (2016).
[14] K. Miwa and H. Ohno, Phys. Rev. Mater. **1**, 053801 (2017).
[15] F. Shimojo, F. Okabe, T. Tachibana, M. Kobayashi, and H. Okazaki, J. Phys. Soc. Jpn. **61**, 2848 (1992).
[16] S. Nosé, Mol. Phys. **52**, 255 (1984).
[17] W. G. Hoover, Phys. Rev. A **31**, 1695 (1985).
[18] R. M. Wentzcovitch, Phys. Rev. B **44**, 2358 (1991).

[19] D. Vanderbilt, Phys. Rev. B **41**, 7892 (1990).
[20] K. Miwa, Phys. Rev. B **84**, 094304 (2011).
[21] Z. Wu and R. E. Cohen, Phys. Rev. B **73**, 235116 (2006).
[22] See Supplemental Material at http://link.aps.org/supplemental/10.1103/PhysRevMaterials.2.105404 for the additional validation.
[23] We have also tried the MD simulation at 300 K. Though the MD run with 150 000 steps was executed, we cannot obtain sufficient statistics.
[24] S. Yu and D. J. Siegel, Chem. Mater. **29**, 9639 (2017).
[25] T. Ikeshoji, E. Tsuchida, T. Morishita, K. Ikeda, M. Matsuo, Y. Kawazoe, and S.-i. Orimo, Phys. Rev. B **83**, 144301 (2011).